Correlating tensile fracture behavior with thermodynamic stability in Fe-P metallic glass

Yuanqi Jiang (蒋元祺)*[a], Rui Zhao(赵瑞) [b], Ping Peng(彭平) [c]

[a] College of Physics & Electronic Information, Nanchang Normal University, Nanchang 330032, China

[b] *School of Mechanical and Electrical Engineering, Xinyu University, Xinyu, 338004, China*

[c] School of Material Science & Engineering, Hunan University, Changsha 410082, China

ABSTRACT:

Despite extensive studies of metallic glasses (MGs), the coupling between thermodynamic evolution, atomic-scale structural rearrangement, and fracture behavior during tensile deformation remains poorly understood, particularly in Fe–P MGs. In this work, molecular dynamics (MD) simulations were performed to investigate the tensile deformation and fracture behavior of Fe–P MGs with different compositions. The results reveal a pronounced non-monotonic compositional dependence of fracture behavior: the toughness decreases with increasing Fe concentration from 14% to 36% and subsequently increases with further Fe enrichment. During the late stage of fracture, atoms bridging the crack surfaces undergo rapid collective clockwise or counterclockwise rotations, accompanied by local structural rearrangement and stress redistribution. Thermodynamic analysis based on an effective Gibbs free-energy framework shows that the free-energy evolution is dominated by mechanically induced enthalpy accumulation under the present low-temperature conditions, while the radial distribution function (RDF)-derived two-body excess entropy provides a structural descriptor of configurational rearrangement. The change of maximum effective free-energy increase, ΔG_{eff}, exhibits a non-monotonic dependence on Fe concentration, increasing from 2.578 eV/atom at $Fe_{14}P_{86}$ to 5.144 eV/atom at $Fe_{73}P_{27}$ and then decreasing to 4.28 eV/atom at $Fe_{84}P_{16}$. Meanwhile, the entropy change exhibits a strongly nonlinear compositional dependence, with relatively large values at $Fe_{14}P_{86}$ and $Fe_{84}P_{16}$ and smaller values at intermediate compositions. These results demonstrate that the tensile fracture behavior of Fe–P MGs is governed by the coupled evolution of mechanically accumulated energy and atomic-scale structural rearrangement, providing a thermodynamic–structural perspective on composition-dependent fracture behavior in metallic glasses.

Keywords: Fe-P, Metallic glass, MD simulation, crack initiation; **PACS:** 81.05.Kf; 62.20.mm; 62.20.Fe; 61.43.Dq

1. Introduction

Metallic glasses (MGs) have attracted increasing attention for engineering applications owing to their exceptional mechanical strength [1], high hardness [2], and superior corrosion resistance [3,4],

*Corresponding author. E-mail: yuanqi325@163.com (Yuanqi Jiang)

making them promising candidates for next-generation structural materials [4,5]. From a fundamental perspective, the successful fabrication of bulk MGs has opened new avenues for addressing key scientific questions in condensed matter physics and materials science [5,6], providing unprecedented opportunities to explore the structural origins of deformation and failure in amorphous systems [5,6]. Among the many unresolved issues in MGs, fracture behavior remains one of the most critical challenges because it directly determines structural reliability [7] and service safety [8]. Unlike crystalline materials, MGs exhibit highly localized deformation [4,7] and complex crack-tip dynamics [7] due to the absence of long-range atomic order, making crack initiation and propagation particularly difficult to predict [4,7]. During fracture, various characteristic nanoscale morphologies, including dimples, nanoscale corrugations, nanospheres, nanowires, and river-like patterns [7], have been observed on fracture surfaces, reflecting the complex deformation processes operating near crack tips [4-8].

In contrast to Cu–Zr MGs, which generally exhibit relatively good ductility [9], Fe–P MGs are a representative intrinsically brittle system [9], especially under phosphorus-rich conditions where brittleness becomes more pronounced [9,10]. Their intrinsic brittleness makes Fe–P MGs as an attractive model system for investigating fracture mechanisms in amorphous materials. In our previous work [10-11], we showed that the spinodal decomposition in rapidly quenched Fe–P MGs is intrinsic rather than an artifact of inaccurate or mismatched interatomic potentials [12], thereby establishing a robust thermodynamic and structural foundation for subsequent fracture studies.

Despite extensive studies [13-17] on the mechanical behavior of MGs, the interplay among composition, thermodynamic stability, and fracture behavior remains insufficiently understood [3,4,9,10], particularly in brittle Fe-based systems. More importantly, the energetic mechanisms governing crack propagation and the ductile-to-brittle transition during tensile deformation remain unclear [7]. In particular, the respective roles of entropy and enthalpy in Gibbs free energy evolution during tensile fracture have yet to be systematically clarified. Motivated by these unresolved issues, the present study systematically investigates the tensile fracture behavior of Fe–P MGs, focusing on how composition influences stability, crack propagation, and mechanical performance [18,19]. Specifically, this work examines the evolution of energy and atomic volume, mechanical properties and toughness, as well as strain- and composition-dependent thermodynamic behavior. By integrating mechanical and thermodynamic analyses, the respective contributions of entropy and enthalpy to Gibbs free energy evolution during tensile fracture are quantitatively evaluated. The results provide new insight into the

fracture mechanisms of Fe–P MGs and the energetic origins of their mechanical behavior, with implications for the design of toughness metallic glass systems.

2. Computational methods

MD simulations were performed using the LAMMPS package [20] to investigate the tensile deformation behavior of $Fe_{84}P_{16}$, $Fe_{73}P_{27}$, $Fe_{64}P_{36}$, $Fe_{50}P_{50}$, $Fe_{36}P_{64}$, and $Fe_{14}P_{86}$ MGs at a strain rate of 0.002 ps^{-1}. The atomic interactions were described using the embedded-atom method (EAM) Fe–P potential developed by Ackland et al. [21], which was originally developed for phosphorus impurities in α-Fe and the associated Fe–P interactions. In the present work, this potential was consistently employed for all investigated Fe–P compositions, from $Fe_{84}P_{16}$ to $Fe_{14}P_{86}$, to enable systematic comparisons under identical simulation conditions. We acknowledge that this potential was not specifically developed to quantitatively reproduce all properties of Fe–P metallic glasses over the entire composition range. Therefore, the absolute values should be interpreted with this limitation in mind, while the emphasis is placed on the relative composition-dependent trends. Importantly, our previous VASP calculations [10,11] showed good agreement with the results obtained using this EAM potential, providing additional support for its applicability to the present Fe–P simulations. Pressure and temperature were controlled using the Parrinello–Rahman barostat [16] and Nosé–Hoover thermostat [17], respectively. To construct the Fe–P MG models, the Fe–P system was first equilibrated at a temperature above its melting point until the total energy reached a stable state, followed by rapid quenching to low temperature [10]. Specifically, a total of 216,000 atoms were randomly placed in a three-dimensional simulation box (431.369 Å × 172.547 Å × 34.5095 Å) under periodic boundary conditions. The initial configuration was subsequently equilibrated in the NVT ensemble at 2300 K to ensure complete melting. The molten Fe–P liquid was then cooled from 2300 K to 1 K within the *NPT* ensemble at a cooling rate of $\gamma = 1 \times 10^{12}$ K/s to suppress crystallization and obtain amorphous Fe–P MGs. To examine fracture behavior, pre-cracked models were generated by removing approximately 1,000~2,000 atoms from the edge region of each Fe–P sample, thereby introducing a triangular crack with dimensions of approximately 20.1 Å × 50.2 Å. Uniaxial tensile loading was subsequently applied perpendicular to the crack surface at a strain rate of 0.002 ps^{-1}. During tensile deformation, periodic boundary conditions were imposed along the y direction, whereas free surfaces were maintained in the x and z directions. The simulation temperature was fixed at 1 K to minimize thermal fluctuations, while the boundaries normal to the crack plane were constrained to suppress Poisson contraction effects [12].

3. Results and discussions

3.1. Potential energy and Volume of Fe-P system

The six Fe_xP_{100-x} systems (x=14,36,50,64,73,84) were rapidly quenched at a cooling rate of $\gamma = 1\times10^{12}$ K/s. Figures 1(a) and 1(b) show the evolution of potential energy and volume of the Fe–P systems as a function of temperature, respectively. As shown in Figure 1(a), all six Fe–P systems exhibit pronounced inflection points in their potential energy curves during rapid cooling, indicative of a glass transition. This is further supported by the clear splitting of the second peak in the radial distribution function (RDF) in Figure 1(c), a characteristic feature of glass transition and amorphization. Based on the inflection points in the potential energy curves, the glass transition temperatures (T_g) of $Fe_{84}P_{16}$, $Fe_{73}P_{27}$, $Fe_{64}P_{36}$, $Fe_{50}P_{50}$, $Fe_{36}P_{64}$, and $Fe_{14}P_{86}$ were determined to be 1001 K, 1016 K, 1002 K, 999 K, 932 K, and 861 K, respectively. Meanwhile, Figure 1(b) shows that the volume of each composition decreases monotonically with decreasing temperature. According to the volume evolution curves, the corresponding T_g values were determined to be 984 K, 999 K, 943 K, 932 K, 876 K, and 861 K, respectively.

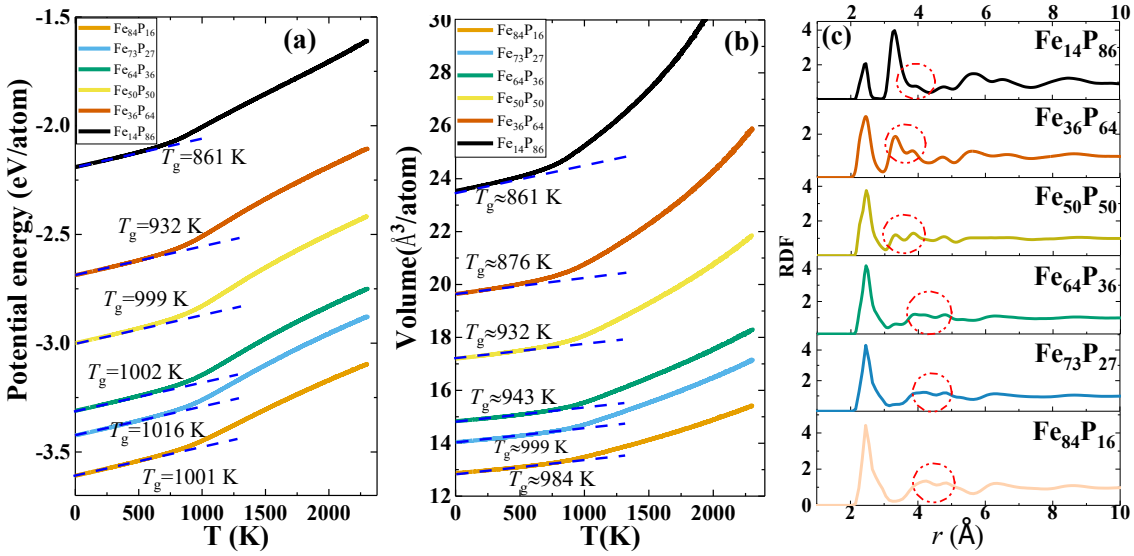


Figure 1. (a) Potential energy (PE) and (b) volume as a function of temperature for Fe_xP_{100-x}(x=14,36,50,64,73,84) MGs, obtained at a cooling rate of γ=1×10^{12} K/s. (c) RDF of these Fe-P MGs at 1 K.

To further clarify the influence of chemical composition on the glass transition temperature of Fe–P MGs, Figure 2 illustrates the relationship between T_g and composition. As shown in Figure 2, regardless of whether T_g is determined from the potential energy (PE) curves or the volume curves, the glass transition temperature increases progressively with increasing Fe content (below 73 % Fe) and decreasing P content. T_g reaches a maximum at 73 % Fe, after which it decreases slightly as the Fe concentration

further increases to 84 %. These results suggest that increasing Fe content generally promotes an increase in T_g in Fe–P MGs.

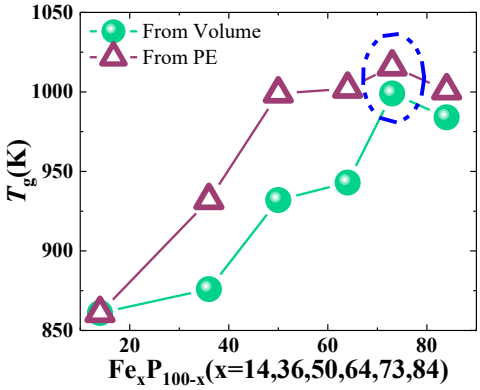


Figure 2. Glass transition temperature (T_g) as a function of the chemical components of Fe_xP_{100-x} (x=14,36,50,64,73,84) MGs with the cooling rate of γ=1×10^{12} K/s.

However, this trend exhibits a critical threshold when the P content becomes excessively low and the system approaches pure Fe, the increase in T_g is no longer sustained.

3.2 Mechanical properties and toughness of Fe–P MGs

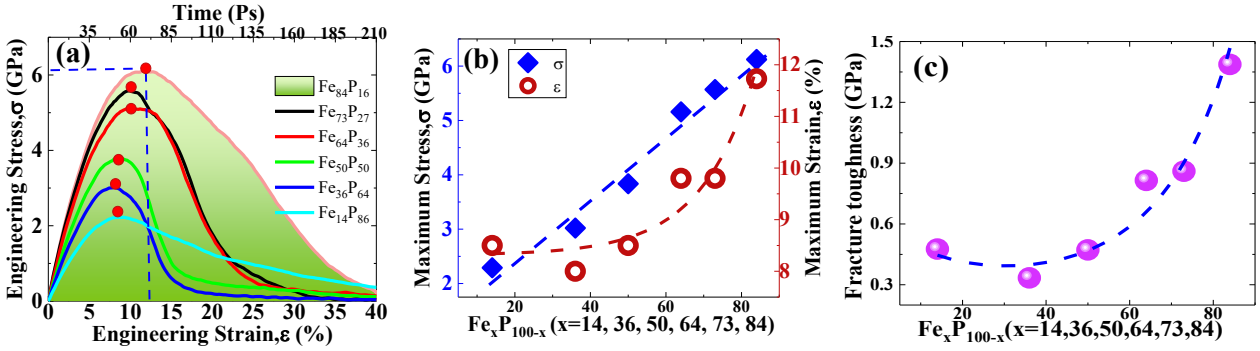


Figure 3. (a) The tensile engineering stress (ES)-engineering strain (ES) curves [10], (b) the dependence of the maximum engineering stress and maximum engineering strain on the Fe content in Fe-P MGs, and (c) the evolution of toughness with the chemical composition of Fe-P MGs. The applied strain rate was 0.002 ps^{-1}.

The tensile stress–strain curves of six Fe–P MGs with different chemical compositions are presented in Figure 3(a) [10]. As shown in Figure 3(a), the tensile deformation behavior of Fe–P MGs can be divided into two distinct stages, separated by the strain corresponding to the maximum tensile stress (marked by small solid red circle at the curve peaks). The first stage corresponds to elastic deformation prior to the peak stress, whereas the second stage begins after the ultimate tensile strength is reached,

during which the system undergoes brittle-like fracture accompanied by rapid stress release. However, at relatively high Fe concentrations, the stress does not drop immediately to zero upon fracture but instead decreases over a finite interval, as exemplified by $Fe_{84}P_{16}$ in Figure 3(a). In contrast, for the other Fe–P MGs compositions

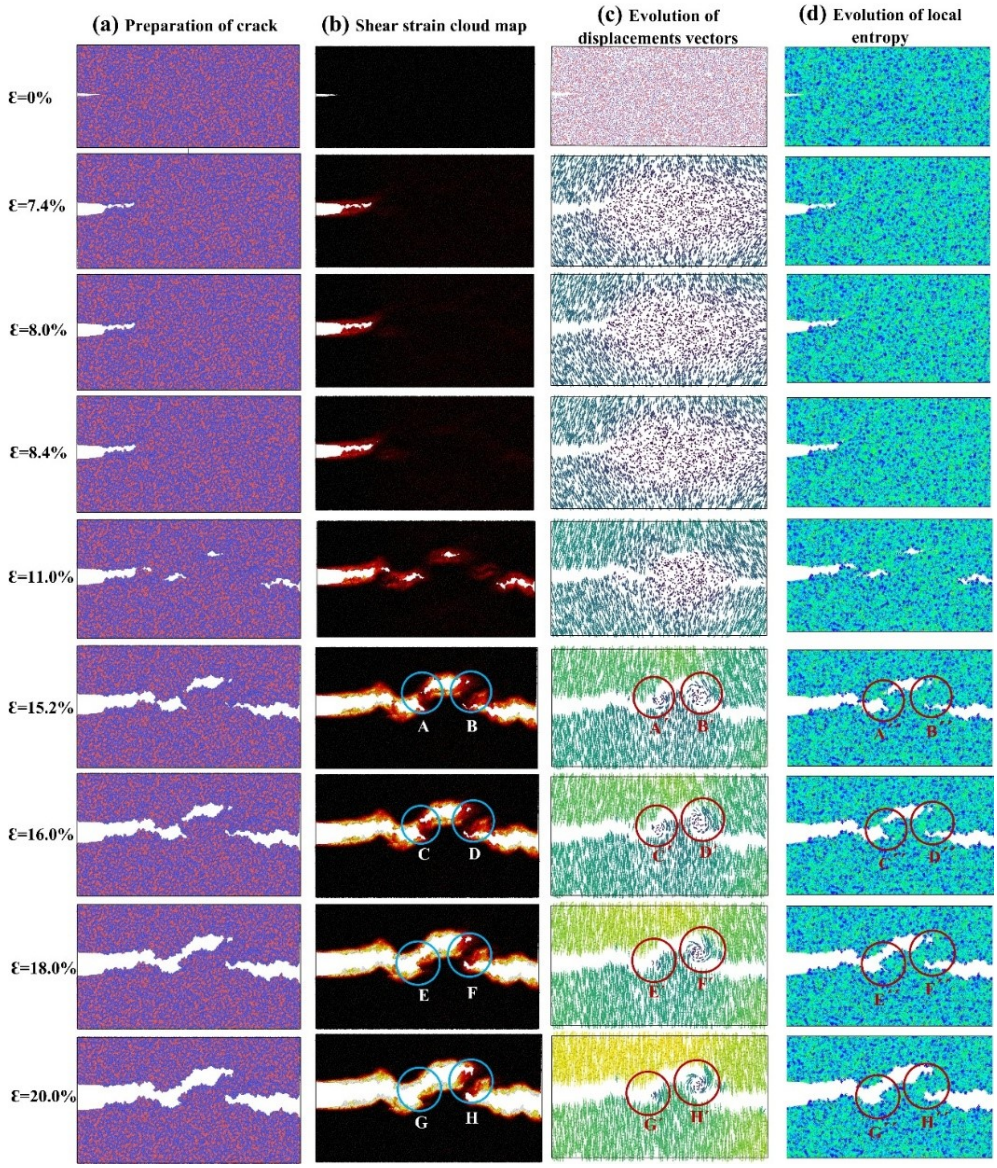


Figure 4. (a) Snapshots of crack propagation, (b) strain contour map, (c) atomic displacement vectors, and (d) the distribution of the local entropy (s_i) of the *i*-th atom during tensile fracture of the $Fe_{50}P_{50}$ metallic glass.

shown in Figure 3(a), the stress rapidly decreases to zero, indicating catastrophic fracture and mechanical failure within an extremely short time scale. Figure 3(b) further illustrates the evolution of peak stress as a function of Fe–P composition (dark blue curve), together with the variation in the critical strain corresponding to the peak stress (red curve). It can be observed that the ultimate tensile stress of Fe–P

MGs increase approximately linearly with increasing Fe content, suggesting that Fe–Fe atomic interactions strongly influence the tensile strength and fracture behavior of the system. Furthermore, beginning with $Fe_{36}P_{64}$, the strain corresponding to the ultimate stress generally increases with increasing Fe content, as shown by the red curve in Figure 3(b).

In our previous investigations of tensile fracture in Al MGs [24], the mechanical toughness was characterized by numerically integrating the area enclosed between the stress–strain curve and the horizontal axis [12,24], as represented by the light green shaded region in Figure 3(a). To some extent, a larger integral value corresponds to a stronger resistance to deformation and fracture [12], whereas a smaller value indicates a greater tendency toward rapid failure over a short time interval. Based on this criterion, Figure 3(c) shows that the toughness decreases significantly from $Fe_{14}P_{86}$ to $Fe_{36}P_{64}$ with increasing Fe content. However, once the Fe concentration exceeds 36 %, the toughness gradually increases with further Fe enrichment. These results further demonstrate that Fe concentration exerts a pronounced influence on the mechanical behavior of Fe–P MGs.

To further elucidate the crack initiation and propagation behavior of Fe–P MGs during tensile fracture from an atomic structural perspective, Figure 4 presents the atomic configurations, strain contour maps, atomic displacement vector fields and the distribution of the local entropy (s_i) of the i-th atom during tensile fracture of $Fe_{50}P_{50}$. As shown in Figure 4, prior to tensile loading, the Fe–P MGs exhibits a pronounced spinodal-like structural feature [10,12]. Compared with the undeformed state, when the strain increases to 7.4 %, the width of the initial crack region becomes noticeably enlarged. Simultaneously, a secondary microcrack emerges ahead of the crack tip, characterized by a relatively narrow width but a length comparable to that of the initial crack. At this stage, a pronounced strain localization region develops near the crack tip. Meanwhile, extensive atomic motions are observed in the region ahead of the crack front (Figure 4(b), Figure 4(c) and Figure 4(d)), although the collective deformation pattern has not yet fully developed as the strain increases from 7.4 % to 8.4 %. Upon further straining to 11.0 %, crack propagation accelerates not only from the original notch but also from the opposite side of the sample. The newly formed crack subsequently propagates toward the initial crack, indicative of unstable brittle fracture behavior. And the strain contour maps in Figure 4(b) further show that the crack boundaries (reddish-brown regions) correspond to regions of highly localized strain. In the remaining atomic ligament regions of the Fe–P MGs (labeled A–F), which persist after crack propagation, the surrounding high-strain regions indicate substantial local deformation concentration. Furthermore, to visually illustrate

this thermodynamic evolution process, we not only further present the atomic displacement vector fields in Figure 4(c), but also simultaneously depict the local entropy (s_i) of the i-th atom as a color scalar in Figure 4(d), together with contour maps showing the spatial distribution of s_i at different tensile strain stages.

For the local entropy (s_i) of the i-th atom in the Fe–P system, it is calculated according to the following equation [25,26]:

$$s_i = -2\pi\rho_i\kappa_B \int_0^\infty [g_i(r)\, ln\, g_i\,(r) - g_i(r) + 1]\, r^2 \cdot dr \quad (1)$$

where ρ is the system's density, and $g_i(r)$ is the RDF. Extensions of the expansion to multicomponent and inhomogeneous systems are also available. Equation (1) gives the two-body excess entropy, which

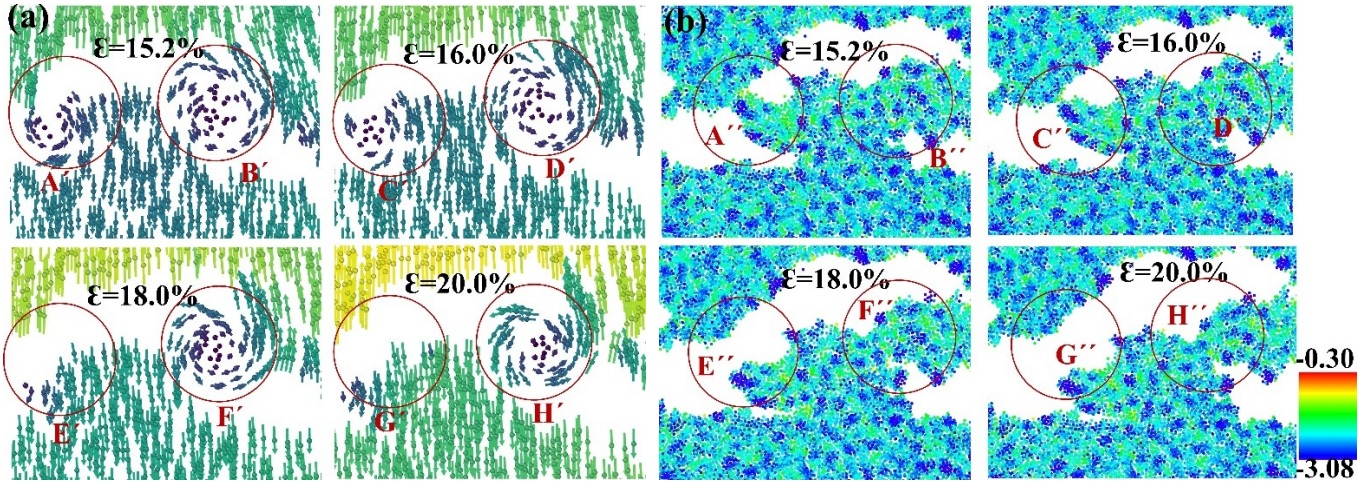


Figure 5. Enlarged views of (a) the evolution of the displacement vectors and (b) the distribution of the local entropy (S_i) of the i-th atom in the red-circled region of Figure 4.

characterizes the contribution of pair correlations to the configurational entropy. In our work, this entropy measure is used primarily as a structural descriptor of atomic-scale disorder and rearrangement during tensile deformation [25,26]. To provide a clearer view of the local atomic motions and s_i distribution during the tensile fracture of the Fe–P metallic glasses, enlarged views of the regions enclosed by the red circles in Figure 4 are further presented in Figure 5. By comparing Figs. 4(c) and 5(a), it can be seen that, when the tensile strain increases to 15.2%, the residual atomic ligament regions do not remain stationary during deformation. Instead, coordinated clockwise and counterclockwise rotational motions are observed in Figure 5(a) (labeled A′–F′). Similar rotation fields, including alternating clockwise and counterclockwise rotational components, have been reported in MGs during localized deformation and

shear-band formation [27,28]. These coordinated rotations are closely associated with the highly heterogeneous stress and strain fields generated during crack propagation. As the crack advances, the material surrounding the crack tip is subjected to a combination of tensile and shear components rather than a purely uniaxial stress state [29]. The resulting stress concentration and heterogeneous deformation generate non-uniform atomic forces within the remaining ligaments, producing local rotational components of the deformation field and facilitating coordinated atomic rearrangements [27–29]. The opposite rotations observed in neighboring parts of the residual ligaments can therefore be regarded as a cooperative response to the local tensile–shear stress field, which enables the ligaments to accommodate deformation while partially relaxing the stress concentration near the advancing crack tip. Importantly, the observed rotation is not an independent deformation mechanism imposed externally, but rather an atomistic response to the local force and stress imbalance associated with crack-tip deformation and ligament constraint.

Regarding the distribution of entropy, Figs. 4(d) and 5(b) show that the spatial distribution of the local entropy (s_i) of the *i*-th atom is highly heterogeneous. Based on the physical meaning of Eq. (1), we find that, during tensile deformation of the Fe–P MGs, the spatial distribution of the s_i does not exhibit a strong positive correlation with crack propagation. In particular, no pronounced high- or low-entropy regions are observed along the crack edges. Notably, after complete fracture, relatively high local structural order, corresponding to the low-entropy regions shown in dark blue, can be observed in some locally protruding regions along the crack edges. However, the spatial extent of these ordered regions is very limited, typically involving only approximately 10–20 atoms. Therefore, the entropy contour maps shown in Figs. 4(d) and 5(b) do not provide a direct or visually discernible indication of the crack propagation process. Instead, they primarily reveal the spatial heterogeneity of local structural order and disorder associated with the atomic arrangements in different regions of the Fe–P metallic glasses. As discussed below, the evolution of the average local entropy per atom ($\bar{s}$) with tensile strain provides a more informative description of the different stages of crack propagation.

3.3 Correlation between thermodynamic descriptors and strain in Fe–P MGs

Based on Eq. (1), the average local entropy per atom ($\bar{s}$) during tensile deformation is calculated as equation (2)

$$\bar{s} = \frac{1}{N}\sum_i^N s_i \quad (2)$$

Where the value of s_i is calculated from Eq. (1), and N is the total number of atoms in the system. In the present work, $\bar{s}$ is used primarily as a structural descriptor of the overall atomic-scale disorder during tensile deformation. The evolution of $\bar{s}$ with tensile strain for the investigated Fe–P MGs is presented in Figure 6. At each strain level, $\bar{s}$ is calculated from the corresponding instantaneous atomic configuration according to Eq. (2). All investigated Fe–P MGs exhibit a similar non-monotonic evolution of $\bar{s}$, characterized by a slight decrease at small strains, followed by a pronounced increase and a subsequent decrease. During the initial elastic stage, the slight decrease in $\bar{s}$ suggests that tensile loading temporarily constrains local atomic configurations and promotes limited structural ordering. With further deformation, $\bar{s}$ increases rapidly, indicating enhanced atomic rearrangement and increasing configurational disorder associated with the development of localized deformation.

For $Fe_{84}P_{16}$, $Fe_{73}P_{27}$, $Fe_{64}P_{36}$, $Fe_{50}P_{50}$, $Fe_{36}P_{64}$, and $Fe_{14}P_{86}$, the maximum values of $\bar{s}$ are reached at tensile strains of 16.00%, 14.29%, 14.30%, 10.83%, 11.07%, and 14.87%, respectively. The subsequent

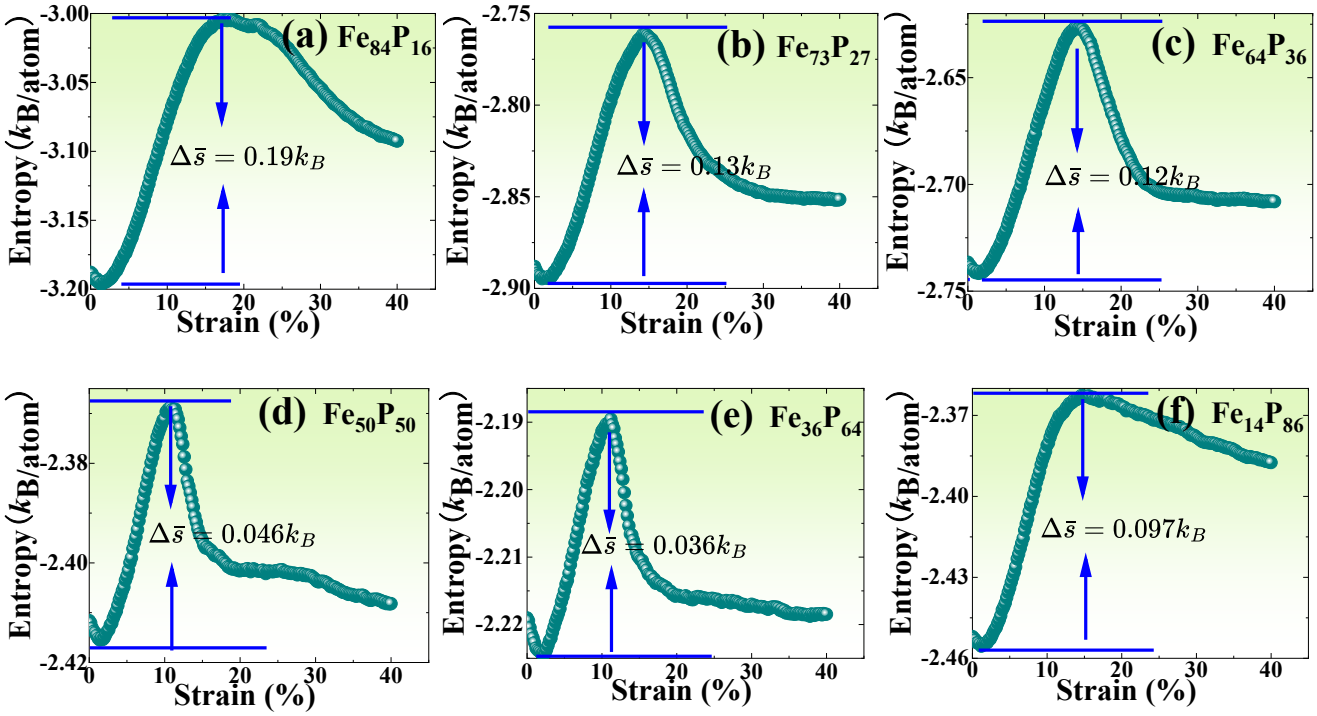


Figure 6. Evolution trend of average entropy per atom ($\bar{s}$) with strain during tensile fracture of Fe-P metallic glass. The entropy changes $\Delta\bar{s} = \bar{s}(\varepsilon)_{max} - \bar{s}(\varepsilon)_{min}$.

decrease in $\bar{s}$ is associated with the transition from distributed structural rearrangement to localized crack propagation and structural separation. Once crack growth becomes dominant, the highly distorted

atomic configurations within the deformation zone are progressively disrupted and reorganized, thereby reducing the spatially averaged pair-correlation contribution to the two-body excess entropy. Thus, the non-monotonic evolution of $\bar{s}$ reflects the competition between configurational disordering during deformation and structural reorganization accompanying fracture, while also being influenced by free-volume evolution [30] and nonequilibrium dissipation [31]. Importantly, although the spatial entropy contour maps in Figs. 4(d) and 5(b) do not directly reveal the propagation of the crack, the strain-dependent evolution of $\bar{s}$ in Figure 6 provides a quantitative description of the structural evolution associated with the different stages of tensile deformation and fracture. In this sense, $\bar{s}$ provides a global thermodynamic descriptor that complements the spatially resolved s_i shown in Figs. 4(d) and 5(b).

To further evaluate the thermodynamic stability during deformation, an effective Gibbs free-energy (G_{eff}) framework was adopted:

$$G_{eff} = (U + PV - T\bar{S}) = H(\varepsilon) - T\bar{S}(\varepsilon) \tag{3}$$

$$\begin{aligned} \Delta G_{eff} &= G(\varepsilon_2) - G(\varepsilon_1) = H(\varepsilon_2) - T\bar{S}(\varepsilon_2) - (H(\varepsilon_1) - T\bar{S}(\varepsilon_1)) \\ &= (H(\varepsilon_2) - H(\varepsilon_1)) - T(\bar{S}(\varepsilon_2) - \bar{S}(\varepsilon_1)) = \Delta H - T\Delta\bar{S} \end{aligned} \tag{4}$$

where G_{eff} and ΔG_{eff} represent the effective Gibbs free energy and its change, respectively, while H,

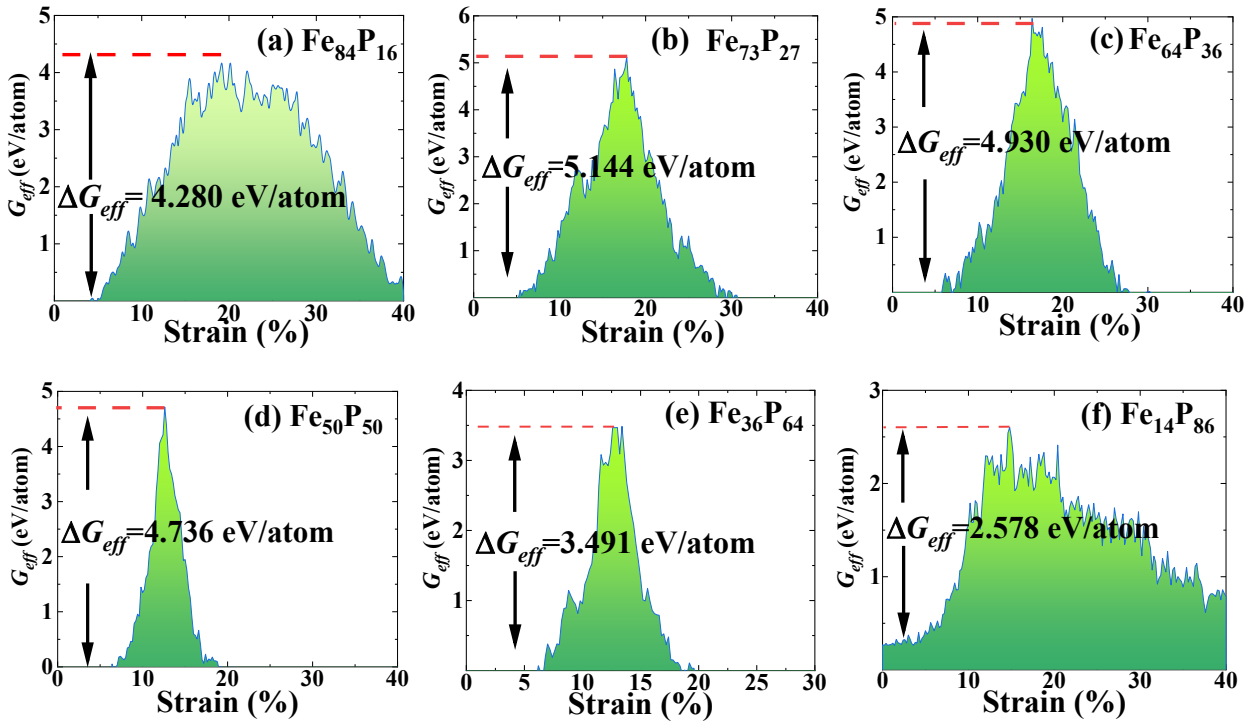


Figure 7. Evolution trend of effective Gibbs free energy (G_{eff}) per atom with tensile strain during tensile fracture of Fe-P metallic glass.

T, and $\bar{S}$ denote the enthalpy, temperature, and average local entropy per atom, respectively. The $\Delta\bar{S}$, is determined from the difference between the maximum and minimum entropy values along the corresponding entropy–strain curve in Figure 6, *i.e.*,

$$\Delta\bar{s} = \bar{s}(\varepsilon)_{max} - \bar{s}(\varepsilon)_{min} \quad (5)$$

For $Fe_{84}P_{16}$, $Fe_{73}P_{27}$, $Fe_{64}P_{36}$, $Fe_{50}P_{50}$, $Fe_{36}P_{64}$, and $Fe_{14}P_{86}$, the $\Delta\bar{s}$ is 0.19 k_B, 0.13 k_B, 0.12 k_B, 0.046 k_B, 0.036 k_B, 0.097 k_B, respectively, in Figure 6. Although these values indicate pronounced entropy variations during tensile deformation, the numerical contribution of the $T\Delta\bar{S}$ remains very small because the temperature is close to 1 K. Even the largest $\Delta\bar{s}$ of 0.19 k_B corresponds to only approximately 1.64×10^{-5} eV/atom for $T\Delta\bar{S}$ at 1 K, which is several orders of magnitude smaller than the mechanically induced enthalpy changes. Therefore, under the present deformation conditions, the evolution of ΔG_{eff} is dominated primarily by mechanically induced enthalpy accumulation, while the entropy term provides only a minor compensating contribution.

In general, lower free energy corresponds to greater thermodynamic stability, whereas higher free energy indicates a greater deviation from an equilibrium-like state. A combined analysis of Figs. 6 and 7 shows that periods of rapid entropy increase are generally accompanied by a substantial increase in effective Gibbs free energy, indicating that the mechanically accumulated enthalpy substantially exceeds the reduction in free energy associated with the $T\bar{S}(\varepsilon)$ term. Consequently, tensile loading progressively drives the Fe–P metallic glasses toward higher-energy metastable states. During the elastic stage, the gradual increase in effective Gibbs free energy indicates that external mechanical work is primarily stored as elastic energy. With further deformation into the inelastic regime, continued free-energy accumulation reflects increasing structural instability and a growing deviation from the initial equilibrium-like state. After the effective Gibbs free energy reaches its maximum, both the entropy and ΔG_{eff} decrease simultaneously, coinciding with extensive crack propagation and the rapid release and redistribution of stored mechanical energy. For example, $Fe_{84}P_{16}$ exhibits a fluctuating high-free-energy plateau over a strain range of approximately 15–25% [Figure 7(a)], suggesting a transient metastable state after shear-band formation and prior to catastrophic failure. Overall, tensile deformation of the Fe–P MGs is governed primarily by mechanically induced enthalpy accumulation, with entropy providing a relatively minor compensating effect on the G_{eff} under the present low-temperature conditions. The combined evolution of G_{eff} and entropy therefore captures the coupling among mechanical energy accumulation,

structural rearrangement and dissipation, and instability-associated energy release during tensile fracture.

3.4. Composition dependence of the ΔG_{eff} and $\Delta\bar{s}$

Building upon the strain-dependent thermodynamic evolution discussed above, the composition dependence of fracture behavior is further examined in terms of the effective free-energy barrier (ΔG_{eff}) and the corresponding entropy change ($\Delta\bar{s}$). Figure 8 summarizes the ΔG_{eff} increase reached during tensile fracture, together with the corresponding entropy changes before and after fracture for the Fe–P MGs. As shown in Figure 8(a), ΔG_{eff} exhibits a pronounced non-monotonic dependence on Fe concentration. With increasing Fe content from 14% to 73%, ΔG_{eff} increases from 2.578 to 5.144 eV/atom. A further increase in Fe concentration to 84% reduces ΔG_{eff} to 4.28 eV/atom.

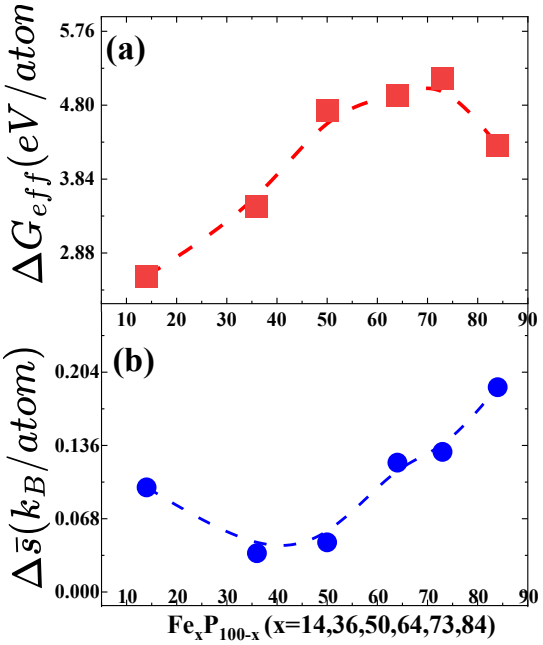


Figure 8. (a) Maximum effective Gibbs free energy barrier per atom (ΔG_{eff}) during tensile fracture of Fe–P MGs and (b) evolution of the change of average entropy per atom ($\Delta\bar{s}$) before and after fracture as a function of Fe–P composition.

Thus, the maximum effective free-energy barrier occurs at 73% Fe. This compositional dependence indicates that the resistance to tensile-induced thermodynamic instability cannot be described by composition-dependent bond strength alone, but is also associated with changes in atomic-scale structural rearrangement. Within the effective Gibbs free-energy framework described by Eqs. (3) and (4), the variation in free energy is determined by the competition between the enthalpic contribution and the entropic contribution. As established above, the $T\Delta\bar{S}$ term is numerically small under the present

low-temperature conditions, and ΔG_{eff} is therefore dominated primarily by mechanically induced enthalpy accumulation. Nevertheless, the composition-dependent entropy change provides useful information about the extent of configurational rearrangement during tensile deformation. As shown in Figure 8(b), $\Delta\bar{S}$ exhibits a strongly nonlinear dependence on Fe concentration.

Relatively large values are observed at both low Fe concentration (14%) and high Fe concentration (84%), whereas substantially smaller values occur in the intermediate composition range of 36–50% Fe. At 14% Fe, the relatively large entropy change ($\Delta\bar{S} = 0.097\, k_B$) is accompanied by the lowest $\Delta G_{eff}(2.578\ \mathrm{eV/atom})$, suggesting that fracture is associated with relatively extensive configurational rearrangement and comparatively limited accumulation of mechanical enthalpy before failure. With increasing Fe concentration to the intermediate regime of 36–50%, $\Delta\bar{S}$ decreases markedly to 0.036~0.046 k_B, whereas ΔG_{eff} increases substantially. This behavior indicates that the accessible atomic rearrangements become more restricted, while a larger amount of mechanical energy can accumulate before the onset of extensive fracture. At 73% Fe, ΔG_{eff} reaches the highest value of 5.144 eV/atom, while $\Delta\bar{S}$ increases to 0.13 k_B, an intermediate value relative to those of the other compositions. This combination indicates that a relatively large amount of mechanical energy can be accumulated before fracture while appreciable, but not maximal, atomic-scale rearrangement occurs. When the Fe concentration is further increased to 84%, $\Delta\bar{S}$ increases sharply to 0.19 k_B, the largest value among the investigated compositions, whereas ΔG_{eff} decreases to 4.28 eV/atom. The simultaneous increase in entropy changes and decrease in ΔG_{eff} suggest that enhanced configurational rearrangement is associated with greater structural accommodation during tensile deformation in the Fe-rich composition. Several structural factors may contribute to this composition dependence. The reduced P concentration may weaken chemical heterogeneity and diminish the stabilizing effect of P-containing short-range motifs [10], while the increased Fe–Fe coordination may promote local structural homogenization and facilitate cooperative atomic rearrangements. These effects may increase the configurational freedom available for structural relaxation and thereby influence the amount of mechanical energy that can be accumulated before fracture. It is important to emphasize that the entropy change shown in Figure 8(b) is derived from the RDF-based two-body excess entropy and represents the change in local structural/configurational disorder during tensile deformation. It should therefore not be interpreted as a directly evaluated activation entropy or used to quantitatively determine a transition-state free-energy barrier. Instead, $\Delta\bar{S}$ provides a structural descriptor that complements the effective free-energy analysis. The observed

composition-dependent correlation between $\Delta\bar{S}$ and ΔG_{eff} indicates that chemical composition affects tensile fracture through the coupled evolution of mechanically accumulated enthalpy and atomic-scale structural rearrangement.

4. Conclusions

In this work, molecular dynamics (MD) simulations were performed to investigate the tensile deformation and fracture behavior of $Fe_{84}P_{16}$, $Fe_{73}P_{27}$, $Fe_{64}P_{36}$, $Fe_{50}P_{50}$, $Fe_{36}P_{64}$, and $Fe_{14}P_{86}$ metallic glasses (MGs). The main conclusions are summarized as follows:

(1) The tensile fracture behavior of Fe–P MGs exhibits a pronounced non-monotonic dependence on composition. The toughness decreases with increasing Fe concentration from $Fe_{14}P_{86}$ to $Fe_{36}P_{64}$ and then increases with further Fe enrichment. Consistently, the maximum effective free-energy increase, ΔG_{eff}, also exhibits a non-monotonic compositional dependence, increasing from 2.578 eV/atom at $Fe_{14}P_{86}$ to 5.144 eV/atom at $Fe_{73}P_{27}$ before decreasing to 4.28 eV/atom at $Fe_{84}P_{16}$. These results indicate that the compositional dependence of fracture behavior is closely associated with the ability of the glass to accumulate mechanical energy prior to failure.

(2) Fracture is accompanied by pronounced atomic-scale structural rearrangements. During the late stage of tensile deformation, atoms bridging the crack surfaces undergo rapid collective clockwise or counterclockwise rotations, accompanied by local structural rearrangement and stress redistribution. These atomic motions provide local structural accommodation during crack evolution and contribute to the deformation process preceding catastrophic failure.

(3) The evolution of effective Gibbs free energy is dominated by mechanically induced enthalpy accumulation under the present low-temperature conditions. Although the RDF-derived two-body excess entropy exhibits substantial composition- and strain-dependent variations, its numerical contribution through the $T\Delta\bar{S}$ term remains small. The evolution of effective free energy therefore primarily reflects the accumulation and subsequent release or redistribution of mechanically stored energy during deformation and fracture.

(4) The composition dependence of fracture behavior arises from the coupled evolution of mechanical energy accumulation and atomic-scale configurational rearrangement. The nonlinear correlation between ΔG_{eff} and the entropy change $\Delta\bar{S}$ highlights the role of configurational evolution in governing tensile fracture of Fe–P MGs.

Data availability statement

The data are available from the corresponding author on reasonable request.

Conflicts of interest

There are no conflicts of interest to declare.

Acknowledgement

The authors acknowledge funding support from National Natural Science Foundation of China (Grants Nos.52263025), the Science and Technology Innovation Team Development Program of Nanchang Normal University (Grant No. NCNUCXTD002), Scientific Research Project of Education Department of Jiangxi Province (Grants Nos. GJJ2202021, GJJ2202011), Qinglan Scholars Program and Scientific Research Project (No.22XJSK04) of Nanchang Normal University. Part of the calculations was performed in the National Supercomputing Center in Tianjin.

Reference:

[1] Tong X, Zhang Y E, Shang B S, Zhang H P, Li Z, Zhang Y, Wang G, Liu Y H, Zhao Y, Zhang B, Ke H B, Zhou J, Bai H Y and Wang W H 2024 *Nat. Mater.* **23** 1193

[2] Zhong L, Wang J, Sheng H, Zhang Z and Mao S X 2014 *Nature* **512** 177

[3] Greer A L 1995 *Science* **267** 1947

[4] Sun B A and Wang W H 2015 *Prog. Mater. Sci.* **74** 211

[5] Cheng Y Q and Ma E 2011 *Prog. Mater. Sci.* **56** 379

[6] Wang W H 2019 *Prog. Mater. Sci.* **106** 100561

[7] Shen L Q, Yu J H, Tang X C, Sun B A, Liu Y H, Bai H Y and Wang W H 2021 *Sci. Adv.* **7** eabf7293

[8] Ji W and Wu M S 2022 *Acta Mater.* **226** 117639

[9] Murali P, Guo T F, Zhang Y W, Narasimhan R, Li Y and Gao H J 2011 *Phys. Rev. Lett.* **107** 215501

[10] Jiang Y Q and Peng P 2025 *J. Phys. Chem. A* **129** 7296

[11] Jiang Y Q and Peng P 2023 *Chin. Phys. B* **32** 047102

[12] He Y, Yi P and Falk M L 2019 *Phys. Rev. Lett.* **122** 035501

[13] Zhang S Y, Tian J, Liu S L, Zhang H M, Bai H Y, Hu Y C and Wang W H 2025 *Natl. Sci. Rev.* **12** nwaf398

[14] Chen Y, Luo X, Ding X, Liu S L, Wang W H and Sun Y H 2026 *Nat. Commun.* **17** 9426

[15] Liu S L, Luo X, Cao J, Liu Z, Xu B B, Sun Y and Wang W H 2023 *Mater. Today Phys.* **38** 101254

[16] Liu S L, Sun Y H, Liu Z and Wang W H 2023 *J. Phys. Chem. C* **127** 21816

[17] Liu S L, Zhang H, Sun B, Sun Y H, Bai H Y and Wang W H 2022 *J. Phys. Chem. Lett.* **13** 754

[18] Shang B S, Wang W H, Greer A L and Guan P F 2021 *Acta Mater.* **213** 116952

[19] Xie Z C, Chen Y, Wang H Y and Dai L H 2021 *Sci. China Technol. Sci.* **64** 1360

[20] Plimpton S 1995 *J. Comput. Phys.* **117** 1

[21] Ackland G J, Mendelev M I, Srolovitz D J, Han S and Barashev A V 2004 *J. Phys.: Condens. Matter* **16** S2629

[22] Gestoso P and Brisson J 2002 *J. Polym. Sci. B* **40** 1601

[23] Martyna G J, Tobias D J and Klein M L 1994 *J. Chem. Phys.* **101** 4177

[24] Jiang Y Q and Peng P 2023 *J. Mater. Res. Technol.* **26** 8997

[25] Piaggi P M, Valsson O and Parrinello M 2017 *Phys. Rev. Lett.* **119** 015701

[26] Piaggi P M and Parrinello M 2017 *J. Chem. Phys.* **147** 114112

[27] Şopu D, Stukowski A, Stoica M and Scudino S 2017 *Phys. Rev. Lett.* **119** 195503

[28] Sepúlveda-Macías M, Gutiérrez G and Lund F 2020 *J. Phys.: Condens. Matter* **32** 174003

[29] Luo J, Huang L, Shi Y and Deng B 2023 *Acta Mater.* **248** 118787

[30] Yang Y, Lu Y, Yang Y, Wang X and An L 2025 *Soft Matter* **21** 5542

[31] Abbasi A, Netz R R and Naji A 2023 *Phys. Rev. Lett.* **131** 228202